PHYSICS

Spin-orbit–coupled exciton-polariton condensates in lead halide perovskites

Michael S. Spencer[1]†, Yongping Fu[1]†, Andrew P. Schlaus[1], Doyk Hwang[1], Yanan Dai[1], Matthew D. Smith[2], Daniel R. Gamelin[2], X.-Y. Zhu[1]*

Copyright © 2021 The Authors, some rights reserved; exclusive licensee American Association for the Advancement of Science. No claim to original U.S. Government Works. Distributed under a Creative Commons Attribution NonCommercial License 4.0 (CC BY-NC).

Spin-orbit coupling (SOC) is responsible for a range of spintronic and topological processes in condensed matter. Here, we show photonic analogs of SOCs in exciton-polaritons and their condensates in microcavities composed of birefringent lead halide perovskite single crystals. The presence of crystalline anisotropy coupled with splitting in the optical cavity of the transverse electric and transverse magnetic modes gives rise to a non-Abelian gauge field, which can be described by the Rashba-Dresselhaus Hamiltonian near the degenerate points of the two polarization modes. With increasing density, the exciton-polaritons with pseudospin textures undergo phase transitions to competing condensates with orthogonal polarizations. Unlike their pure photonic counterparts, these exciton-polaritons and condensates inherit nonlinearity from their excitonic components and may serve as quantum simulators of many-body SOC processes.

INTRODUCTION

Spin-orbit coupling (SOC) of electrons is responsible for a number of quantum phenomena in solids, including spin Hall effect (*1*) and topological insulators (*2*). These SOC phenomena also emerge in photonic systems (*3*–*8*). In planar microcavities, the natural splitting between transverse electric (TE) and transverse magnetic (TM) modes behaves as a winding in-plane magnetic field $\vec{B}_T$ on the photon spin and results in the photonic spin Hall effect (*4*–*6*). If in-plane optical anisotropy is present to break rotational symmetry (*9*), there is an effectively constant magnetic field $\vec{B}_{XY}$ which, in combination with $\vec{B}_T$, leads to a non-Abelian gauge field for photons or exciton-polaritons near the so-called diabolical point, where the fields cancel (*10*). There have been increasing interests in recent years to introduce SOC directly via engineering a photonic system to exhibit optical analogs of SOC and topological effects from pseudo-magnetic fields and/or pseudospins (*11*–*13*). While these photonic systems have been demonstrated for synthetic Rashba-Dresselhaus Hamiltonians (*3*, *8*, *14*–*16*), an exciting prospect is forming exciton-polariton condensates (*17*, *18*) under such an effective field to simulate a number of phenomena in SOC quantum fluids (*10*), in analogy to what have been demonstrated in SOC Bose-Einstein condensates (BECs) in cold atoms (*19*–*21*). Here, we demonstrate spin-polarized exciton-polaritons and condensates in microcavities composed of single-crystal lead halide perovskites (LHPs) (*22*) known for strong light-matter coupling in microcavities (*23*–*27*), including topological photonic structures (*27*, *28*). We take advantage of low-symmetry phases of LHPs with strong optical anisotropy, which is tunable by composition and/or temperature (*29*), and measure the spin textures produced by $\vec{B}_T + \vec{B}_{XY}$ using polarization resolved Fourier space photoluminescence (FS-PL) imaging. In the present study, we focus on two regions in the in-plane momentum space ($k_\parallel$): (i) the region near the so-called diabolic point (k_{db}) where $\vec{B}_T$ and $\vec{B}_{XY}$ cancel each other and the Hamiltonian is of the Rashba-Dresselhaus form; and (ii) the region near $k_\parallel = 0$ where condensates form from the spin-polarized exciton-polaritons as their density reaches a threshold. The present study will not probe propagating condensates near k_{db}; this will be subject of future studies.

In a planar distributed Bragg reflector (DBR) cavity with the presence of TE-TM splitting and optical anisotropy, the Hamiltonian describing the eigenstates in a circular polarization basis is given by (*7*, *10*)

$$\boldsymbol{H}_{\mathrm{Ph}} = \begin{pmatrix} E_0 + \frac{\hbar^2 {k_\parallel}^2}{2m} & -\alpha e^{-i\phi_0} + \beta {k_\parallel}^2 e^{-2i\phi} \\ -\alpha e^{i\phi_0} + \beta {k_\parallel}^2 e^{2i\phi} & E_0 + \frac{\hbar^2 {k_\parallel}^2}{2m} \end{pmatrix} \quad (1)$$

where the degenerate diagonal terms are cavity photon modes. $k_\parallel$ is in-plane momentum with propagation angle φ, $\boldsymbol{k}_\parallel = (k_\parallel \cos\varphi, k_\parallel \sin\varphi)$; E_0 is the mode energy at $k_\parallel = 0$ and m the cavity reduced mass for a given mode; $\beta {k_\parallel}^2$ and α represent the strength of TE-TM splitting and optical anisotropy, respectively; and φ_0 is the fixed in-plane angle of $\vec{B}_{XY}$ with respect to the optical axis. As a 2 × 2 Hermitian Hamiltonian, Eq. 1 can be decomposed into a linear combination of Pauli matrices, which can be viewed as Zeeman interaction between an effective magnetic field and the pseudospin of a photon (text S1) (*7*)

$$\boldsymbol{H}_{\mathrm{Ph}}(\boldsymbol{k}_\parallel) = \left(E_0 + \frac{\hbar^2 k_\parallel^2}{2m}\right)\mathbb{1} + \vec{\boldsymbol{G}}(\boldsymbol{k}_\parallel)\cdot\vec{\boldsymbol{\sigma}} \quad (2)$$

where $\mathbb{1}$ is the 2 × 2 unit matrix, $\vec{\boldsymbol{\sigma}}$ is a vector of Pauli Matrices, and $\vec{\boldsymbol{G}}(\boldsymbol{k}_\parallel) = (-\alpha\cos(\phi_o) + \beta k_\parallel^2 \cos(2\phi), -\alpha\sin(\phi_o) + \beta k_\parallel^2 \sin(2\phi), 0)$ is the effective magnetic field given by the sum of $\vec{\boldsymbol{B}}_{XY}$ and $\vec{\boldsymbol{B}}_T$. The pseudospins of the eigenstates are either aligned or antialigned with the effective field. The $k_\parallel$-dependent effective field acting on the photon pseudospin can be physically interpreted as a photonic SOC around the diabolic points.

RESULTS AND DISCUSSIONS

We directly grow single-crystal microplates of $MAPbBr_3$ [MA (methylammonium)] or $CsPbBr_3$ perovskites in an empty cavity formed

[1]Department of Chemistry, Columbia University, New York, NY 10027, USA. [2]Department of Chemistry, University of Washington, Seattle, WA 98195-1700, USA.
*Corresponding author. Email: xyzhu@columbia.edu
†These authors contributed equally to this work.

by two laminated DBRs (Fig. 1, A and B). The natural thickness gradient of the microcavities allows us to tune the cavity resonances across the exciton resonance (E_{ex}). The as-grown single crystals exhibit 10 to 100 μm in lateral dimensions and a few micrometers in thickness. Additional optical images (fig. S1), powder x-ray diffraction (fig. S2), atomic force microscopy (fig. S3), and reflectance spectra (fig. S4) of representative samples are provided in the Supplementary Materials. At room temperature, $CsPbBr_3$ is in the birefringent orthorhombic structure, whereas $MAPbBr_3$ is in the isotropic cubic structure (*29*), and this difference results in distinctive dispersions with pseudospin textures of the resulting polaritons.

We perform FS-PL imaging on the microcavities (fig. S5) to obtain dispersion in parallel momentum, $\boldsymbol{k}_{\parallel} = (k_x, k_y)$. Constant-energy cross sections in the energy-momentum space are shown in Fig. 1 (C and D, respectively) for $MAPbBr_3$ and $CsPbBr_3$ and in movies S1 and S2). The effective cavity lengths support multiple longitudinal Fabry-Pérot modes. The modes of cubic $MAPbBr_3$ are perfectly concentric in $k_{\parallel}$ (Fig. 1C). By contrast, optical anisotropy in $CsPbBr_3$ splits each mode into two ellipses that are degenerate at certain momentum points. The dispersion of the isotropic $MAPbBr_3$ microcavity is characterized by two orthogonal polarization modes degenerate at $k_{\parallel} = 0$ but split at higher $k_{\parallel}$ (fig. S6), indicating the presence of the winding $\vec{B}_T$ only. By comparison, in-plane anisotropy in $CsPbBr_3$ leads to a clear mode splitting at $\boldsymbol{k}_{\parallel} = 0$ due to $\vec{B}_{XY}$ (Fig. 1E). As the cubic $MAPbBr_3$ undergoes phase transitions at lower temperature, the dispersion markedly changes (fig. S7). The tetragonal phase exhibits a small mode splitting due to a finite anisotropy, whereas the orthorhombic phase shows much larger $\boldsymbol{k}_{\parallel} = 0$ splitting that is even larger than those in $CsPbBr_3$.

The high quality factor ($Q = 970 \pm 100$, derived from the polariton linewidth below condensation threshold; fig. S8) of our microcavities ensures sufficient coupling of the excitons to the photonic

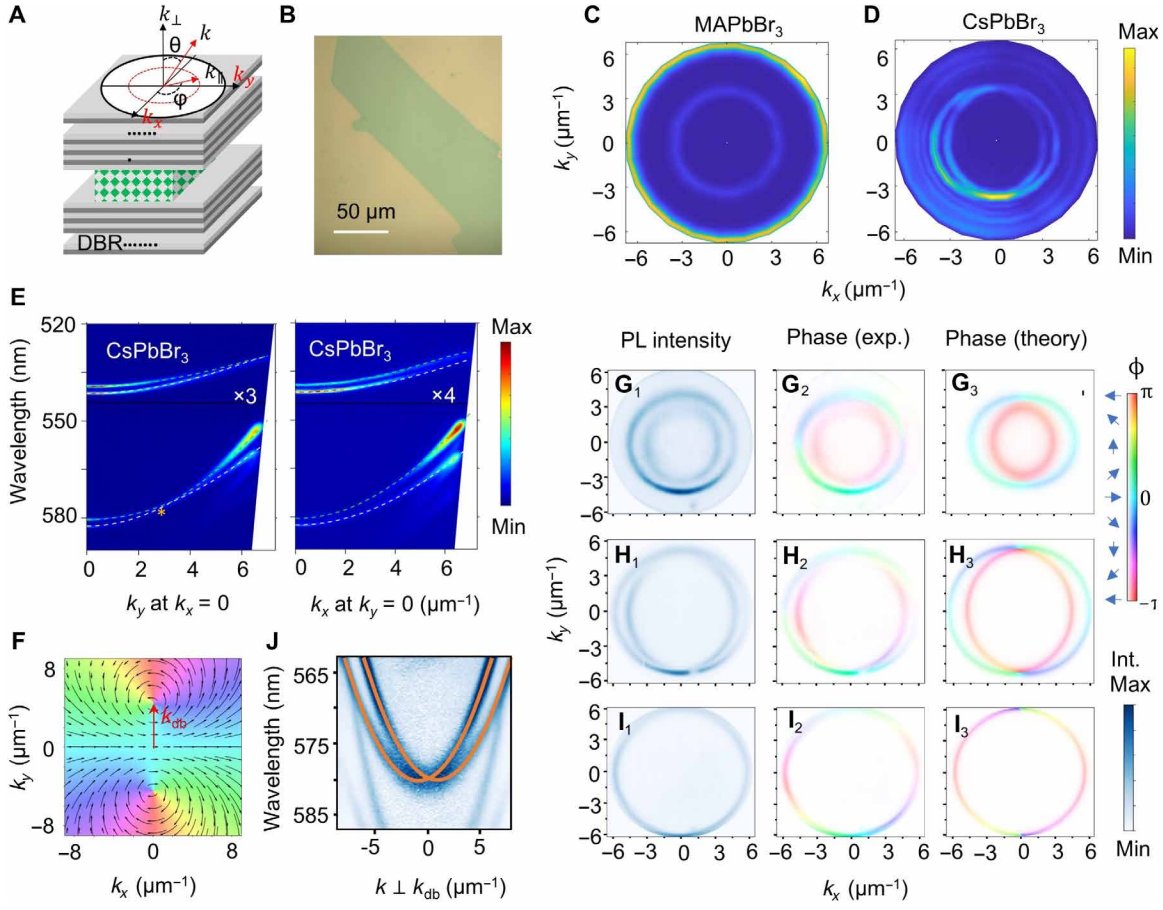

Fig. 1. Spin textures in the anisotropic $CsPbBr_3$ perovskite microcavities. (**A**) Schematic (left) and optical image of a $CsPbBr_3$ microcavity formed by two DBRs. The in-plane momentum is $k_{\parallel} = \frac{2\pi}{\lambda}\sin\theta$; θ is the polar angle of emission and λ is the emission wavelength. ϕ is the azimuthal angle in the plane. (**B**) Optical image of a $CsPbBr_3$ single crystal grown in the microcavity channel. (**C**) Constant-energy cross section at emission wavelength 565 nm from an isotropic $MAPbBr_3$ microcavity, showing a circular ring. (**D**) Constant-energy cross section at 574.5 nm from an anisotropic $CsPbBr_3$ microcavity showing two offset circular modes. k_x and k_y are aligned with the ⟨100⟩ directions of the (pseudo-)cubic perovskite structures ($\phi_o = 0°$). (**E**) Dispersions along the k_x and k_y in the $CsPbBr_3$ microcavity, showing degeneracy at particular k_y (marked by *) and anisotropic mode splitting at $\boldsymbol{k}_{\parallel} = 0$. The dashed curves are theoretical SOC exciton-polaritons from Eq. 4. (**F**) The momentum distribution of the effective magnetic field or gauge field and the Stokes polarization vectors parallel or antiparallel to $\vec{B}_{eff}$. k_{db} is the wave vector where the effective magnetic field vanishes. ($\mathbf{G}_1$), ($\mathbf{H}_1$), and ($\mathbf{I}_1$) show cuts of experimental dispersions at energies below (553.0 nm), at (548.9 nm), and above (544.7 nm) the diabolical points, respectively. (G_2), (H_2), and (I_2) are the corresponding experimental spin textures, and (G_3), (H_3), and (I_3) are the corresponding theoretical spin textures from the Rashba-Dresselhaus Hamiltonian. (**J**) The energy dispersion intersecting the diabolical point in the direction perpendicular to k_{db}, showing two offset parabolas.

modes, forming SOC polaritons. Diagonalization of the Hamiltonian (Eq. 1) gives two φ-dependent SOC photonic modes (*10*)

$$E_{\mathrm{ph}\pm}(\boldsymbol{k}_\parallel) = E_0 + \frac{\hbar^2 k_\parallel^{\,2}}{2m} \pm \sqrt{\beta^2 k_\parallel^{\,4} - 2\alpha\beta k_\parallel^{\,2}\cos(2\varphi - \phi_o) + \alpha^2} \quad (3)$$

When the SOC cavity photons are strongly coupled to an exciton resonance with Rabi splitting Ω, and neglecting the difference in the exciton energies of the two orthogonal polarizations (fig. S9), we obtain two spin-split lower polariton branches (LPBs) and two spin-split upper polariton branches, which are given by

$$E_{\mathrm{Pol}}(\boldsymbol{k}_\parallel) = \frac{E_{\mathrm{ex}} + E_{\mathrm{ph}\pm}(\boldsymbol{k}_\parallel)}{2} \pm \frac{1}{2}\sqrt{[E_{\mathrm{Ph}\pm}(\boldsymbol{k}_\parallel) - E_{\mathrm{ex}}]^2 + \Omega^2} \quad (4)$$

Because the effective field depends exclusively on the momentum vector, not on the energy, the spin texture of each photon mode is preserved in the polariton mode (fig. S10 and text S2).

The excitonic and photonic fractions depend on the cavity detuning $\delta = E_0 - E_{\mathrm{ex}}$. When $|\delta| > \Omega$, the polariton modes are more photon-like for the momentum space in our imaging range, and the energy dispersion can be described by Eq. 3, as shown by dashed curves on the lower-energy modes in Fig. 1E. For these modes, the polariton emission strongly increases toward E_{ex} at high k because of the relaxation bottleneck (*30*). Along k_y Fig. 1E (left), the two anisotropic modes cross at $k_y = \pm(\alpha/\beta)^{0.5} = \pm 3.3\ \mu\mathrm{m}^{-1}$, i.e., the diabolical points (k_{db}) where $\vec{B}_{XY}$ and $\vec{B}_T$ cancel each other. Along k_x (Fig. 1E, right), the two fields add up, and the energy splitting increases with k_x. We reproduce the two dispersions using Eq. 3 with $E_0 = 2132.4 \pm 0.6$ meV, $\frac{\hbar^2}{2m} = 2.24 \pm 0.08$ meV μm^{-2}, $\beta = 0.34 \pm 0.03$ meV μm^{-2}, and $\alpha = 7.4 \pm 0.8$ meV. The two modes are orthogonally polarized (figs. S11 and S12), and the pseudospins switch across the diabolical points.

As shown in Fig. 1F, the addition of $\vec{B}_{XY}$ (green arrows) to $\vec{B}_T$ (orange arrows) breaks the rotational symmetry of the TE-TM doublets (*31*), separating the TE-TM of 4π winding into a pair of two-dimensional (2D) monopoles of 2π winding. The effective magnetic field vanishes at the angles corresponding to $\varphi = \phi_o/2$, and at wave vectors $\boldsymbol{k}_{\mathrm{db}} = \sqrt{\alpha/\beta}\left(\cos\frac{\phi_o}{2}, \sin\frac{\phi_o}{2}\right)^T$, giving rise to the diabolical points. In the region near these points, the Hamiltonian (Eq. 1) can be rewritten (text S3) as a Rashba-Dresselhaus Hamiltonian (*10*)

$$\boldsymbol{H}_{\mathrm{Ph}}(\boldsymbol{k}_\parallel = \boldsymbol{k}_{\mathrm{db}} + \boldsymbol{q}) \approx \left(E_o + \frac{\hbar^2(\boldsymbol{k}_{\mathrm{db}} + \boldsymbol{q})^2}{2m}\right)1 + \beta\boldsymbol{q}^2 + 2\sqrt{\alpha\beta}\left[\cos\left(\frac{\phi_o}{2}\right)\boldsymbol{\sigma}\cdot\boldsymbol{q} + \sin\left(\frac{\phi_o}{2}\right)\boldsymbol{\sigma}\times\boldsymbol{q}\right] \quad (5)$$

where $\boldsymbol{q} = \boldsymbol{k}_\parallel - \boldsymbol{k}_{\mathrm{db}}$. Note that it is within this context that the effective magnetic field produces a non-Abelian gauge field, whereas in general it is an effective magnetic field. For our spin-split polariton modes where the diabolic points are within the measurable $k_\parallel$ range, we compare the experimental pseudospin textures with predictions from the Hamiltonian (Eq. 1). We map the Stokes vectors of the two polariton eigenstates and plot their $\boldsymbol{k}_\parallel$-dependent phases $\phi_{\mathrm{Stokes}} = \tan^{-1}(S_2/S_1)$, where S_1 and S_2 are the Stokes parameters on the Poincaré sphere (text S4). We also note that the dispersions near the diabolic point resemble the behavior near the Dirac point in graphene, with an additional slope. The Hamiltonian in (Eq. 5) is similar to the tight binding Hamiltonian of graphene, except with an additional "twist," which reflects the fact that the gauge field can be written as a divergence, a curl, or some combination of the two, depending on the crystal angle (ϕ_o) (see text S3).

We show constant-energy cuts of PL intensity (Fig. 1, G_1, H_1, and I_1), phase (Fig. 1, G_2, H_2, and I_2), and theoretical phase (Fig. 1, G_3, H_3, and I_3) at energies below (Fig. 1G), at (Fig. 1H), and above (Fig. 1I) the diabolical points, where $|\vec{B}_{XY}| > |\vec{B}_T|$, $\vec{B}_{XY} = -\vec{B}_T$, and $|\vec{B}_{XY}| < |\vec{B}_T|$, respectively. In all three regions, the experimentally retrieved pseudospin textures agree with the theoretical predictions from Hamiltonian (Eq. 1). In the *XY*-dominant regime, a nearly constant magnetic field generates Zeeman splitting, giving rise to two modes polarized along $\phi \sim \phi_o$ and $\sim\phi_o + \frac{\pi}{2}$, respectively. In the TE-TM dominant regime, the two modes show the expected 4π phase winding. At the energy of the diabolical points, exchanging the interior and exterior degenerate eigenstates across the diabolical points gives rise to two circular rings with exactly 2π phase windings. One can observe the pseudospin points to opposite directions at each side of the points, which agrees with the Rashba-Dresselhaus field. Moreover, the Rashba energy structure is confirmed in Fig. 1J, which displays the measured dispersion intersecting the diabolical point in the direction perpendicular to $\boldsymbol{k}_{\mathrm{db}}$. The two spin-split parabolas can be well described by the theoretically predicted $E_\pm \approx E(\boldsymbol{k}_{\mathrm{db}}) + \frac{\hbar^2 q^2}{2m} \pm 2\sqrt{\alpha\beta}\boldsymbol{q}$ (the solid lines in Fig. 1J). The anisotropic splitting from $\vec{B}_{XY}$ in $MAPbBr_3$ in the low-temperature orthorhombic phase (fig. S13) is even stronger than that in $CsPbBr_3$; both are two orders of magnitude higher than those in GaAs and CdTe microcavities (*7*, *32*, *33*). The magnitudes of Rashba-Dresselhaus splitting of the exciton-polaritons in our LHP microcavities are at levels previously only seen for pure photonic modes (*3*, *8*). Unlike the reported SOC photonic modes that have no matter components and therefore no nonlinearity (*3*, *8*), the SOC exciton-polaritons in our LHP microcavities are highly nonlinear and undergo phase transitions to competing condensates, as we establish below.

For polaritons with E_0 close to E_{ex}, we observe deviations from parabolic dispersions at high k and avoided crossings with the exciton resonance, as seen for both $MAPbBr_3$ (fig. S6) and the $CsPbBr_3$ microcavities (Fig. 1D and fig. S14 at different δ values). The dispersions can be reproduced by the LPBs in Eq. 4 with $E_0 = 2296.4 \pm 0.6$ meV, $\frac{\hbar^2}{2m} = 1.08 \pm 0.05$ meV μm^{-2}, $\beta = 0.10 \pm 0.01$ meV μm^{-2}, $\alpha = 10 \pm 1$ meV, and $\Omega = 12 \pm 2$ meV, giving rise to diabolical points at $k_y \sim 7.1\ \mu\mathrm{m}^{-1}$. The two polariton modes are orthogonally polarized (figs. S11 and S12), in agreement with a report by Bao *et al.* (*25*) on a $CsPbBr_3$ microcavity. Note that these authors did not observe diabolic points, spin textures, or phase transition into competing condensates.

Polariton formation becomes more obvious at lower temperatures, shown here by dispersions from a $CsPbBr_3$ microcavity at $T = 77$, 120, 200, and 290 K, respectively (Figs. 2, A_1 to A_4, and fig. S15). The dispersions of the LPBs closest to E_{ex} are flattened at large $\boldsymbol{k}_\parallel$ because of avoided crossing. Our modeling with Eq. 4 yields $\Omega = 25 \pm 3$, 25 ± 3, 18 ± 2, and 16 ± 2 meV for this cavity at 77, 120, 180, and 290 K, respectively. The strong coupling is further supported by a clear cavity detuning effect seen in fig. S16, which shows a series of dispersions for positive, resonant, and negative detuning. The polariton modes inherit the spin textures from the cavity photon modes, as shown by the dispersions at 77 K of horizonal (Fig. $2B_1$), vertical (Fig. $2B_2$), and 45° (Fig. $2B_3$) polarizations. Polarization angular dependences of the two polariton modes near E_{ex} (Fig. $2B_4$) confirm that the two spin-split polariton modes have orthogonal polarizations.

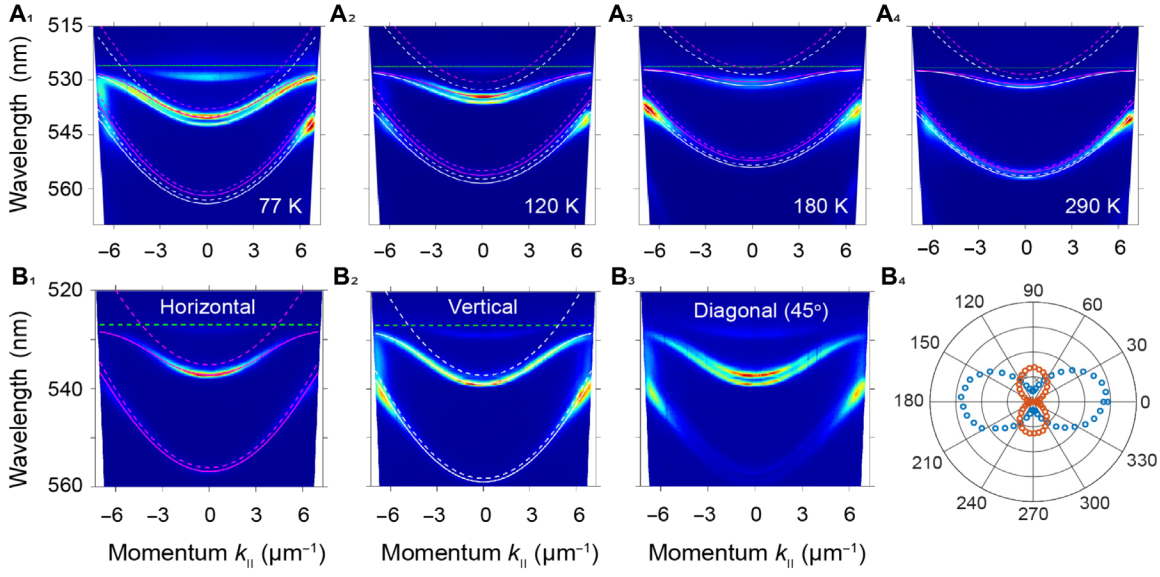

Fig. 2. Temperature-dependent and polarization-resolved dispersions in $CsPbBr_3$ microcavities. (**A**) Dispersion of a $CsPbBr_3$ microcavity measured at 77 K (A_1), 120 K (A_2), 180 K (A_3), and 290 K (A_4). Dashed lines are the expected optical cavity dispersions; solid lines are the modeled polariton dispersions. The corresponding Rabi splittings are 25 ± 3, 25 ± 3, 18 ± 2, and 16 ± 2 meV, respectively. (**B**) Polarization-resolved dispersions of a $CsPbBr_3$ microcavity at 77 K. The polarization is (B_1) horizontal, (B_2) vertical, and (B_3) diagonal, with respect to the direction of the entrance slit in front of a spectrometer. (B_4) Polarization-resolved PL emission of the two anisotropic modes ~538 nm at $k_{\parallel} = 0$, showing that the two modes are mutually orthogonal and linearly polarized.

The coupling constant Ω obtained here is more than a factor of 2 smaller than the Ω = 60 meV reported by Su *et al.* (*24*) for a room temperature $CsPbBr_3$ microcavity. In addition to differences in cavity structure and crystal growth procedures between our work and that of Su *et al.*, the different Ω values may likely come from the different E_{ex} values used. We use E_{ex} = 2.353 ± 0.005 eV in our analysis. By examining the dispersions at different cavity detuning in our wedged samples, we consistently observe the avoided crossing at E_{ex} = 2.353 ± 0.005 eV. Note that, unlike the nearly constant PL peak energy, the absorption peak energy blue-shifts with increasing temperature (*34*), as is confirmed in our reflectance spectra (fig. S4). This blue shift is also accompanied by notable peak broadening with temperature, giving rise to large uncertainty in the determination of E_{ex} at room temperature. If we use the same E_{ex} = 2.407 eV as in (*24*), our fitting yields Ω = 50 ± 5 meV, in closer agreement with Su *et al.* (*24*).

Having established the SOC exciton-polariton modes with spin textures, we now turn to their phase transitions into competing condensates. Figure 3 (A to C) shows PL spectra at 77 K as functions of pump fluence (P) and the calculated exciton density (n_{ex}; text S4) for $CsPbBr_3$ microcavities with increasing detuning δ = E_0 − E_{ex} = +1, −15, and −40 meV, respectively. For the most resonant cavity, δ = 1 meV (Fig. 3A), we observe two thresholds in the appearance of sharp PL peaks assigned to lasing, at P_{th1} = 5.0 ± 0.3 μJ cm^{-2} and P_{th2} = 53 ± 3 μJ cm^{-2}, corresponding to n_{ex} ~ 1 × 10^{17} and ~1 × 10^{18} cm^{-3}, respectively. With increased detuning, δ = −15 meV (Fig. 3B), the two lasing thresholds up-shift to P_{th1} = 8.6 ± 0.4 μJ cm^{-2} and P_{th2} = 84 ± 4 μJ cm^{-2}. For the largest detuning, δ = −40 meV (Fig. 3C), there is mainly one threshold that is slightly different for the two SOC modes, P_{th1_a} = 10.6 ± 0.5 μJ cm^{-2} and P_{th1_b} = 13.2 ± 0.7 μJ cm^{-2} at ~537 and ~540 nm, respectively. The insets in Fig. 3 (A to C) show representative spectra, black, blue, and red (or green), for $P < P_{th1}$, $P_{th1} < P < P_{th2}$ (or $P_{th1\_a} < P < P_{th1\_b}$), and $P > P_{th2}$ (or $P > P_{th1\_b}$), respectively. For $P < P_{th1}$, the broad spectrum (525 to 550 nm) is spontaneous emission, and the linewidth of the polariton is 0.55 nm. For δ = +1 or −15 meV, a sharp lasing peak in one or both SOC modes at ~533 nm appears with a two–orders of magnitude decrease in full width at half maximum (FWHM) to 0.21 ± 0.01 nm, corresponding to an effective quality factor of Q = 2500. When $P > P_{th2}$, two additional lasing peaks emerge at the lower-energy cavity modes (~547 nm). For the largest detuned cavity, δ = −40 meV, the second threshold for the red-shifted lasing modes is not observed within the fluence range. Instead, we observe the lower SOC mode appearing slightly delayed and increasing after the higher SOC mode has saturated.

A two-threshold lasing behavior has been considered as strong evidence for exciton-polariton condensation: The first is attributed to stimulated scattering to form the condensates, also called polariton lasing (*17*, *18*), and the second, at density above the Mott threshold, to stimulated emission from electron-hole (e-h) plasmas (*35*–*39*). Polariton lasing requires the system to remain in strong coupling. With increasing n_{ex}, many-body screening reduces the exciton binding energy, causing the system to undergo Mott transition to an e-h plasma with a reduction of the oscillator strength and resulting in weak coupling to photons (*40*). The Mott density in single-crystal $CsPbBr_3$ or $MAPbBr_3$ is n_{Mott} ~ 8 × 10^{17} cm^{-3} (*40*, *41*). Thus, P_{th1} is far below n_{Mott}, while P_{th2} is within a factor of 2 to 4 (depending on detuning) above n_{Mott}. The second lasing threshold may be related to the Bardeen-Cooper-Schrieffer (BCS) polariton lasing, a mechanism predicted theoretically (*42*–*44*) and more recently demonstrated experimentally in a GaAs quantum well microcavity (*39*). In the BCS mechanism, the e-h pair is no longer tightly bound as in the exciton but Coulomb correlated to form a BCS-like pair (*39*) in the so-called nondegenerate e-h plasma (*40*). As the exciton

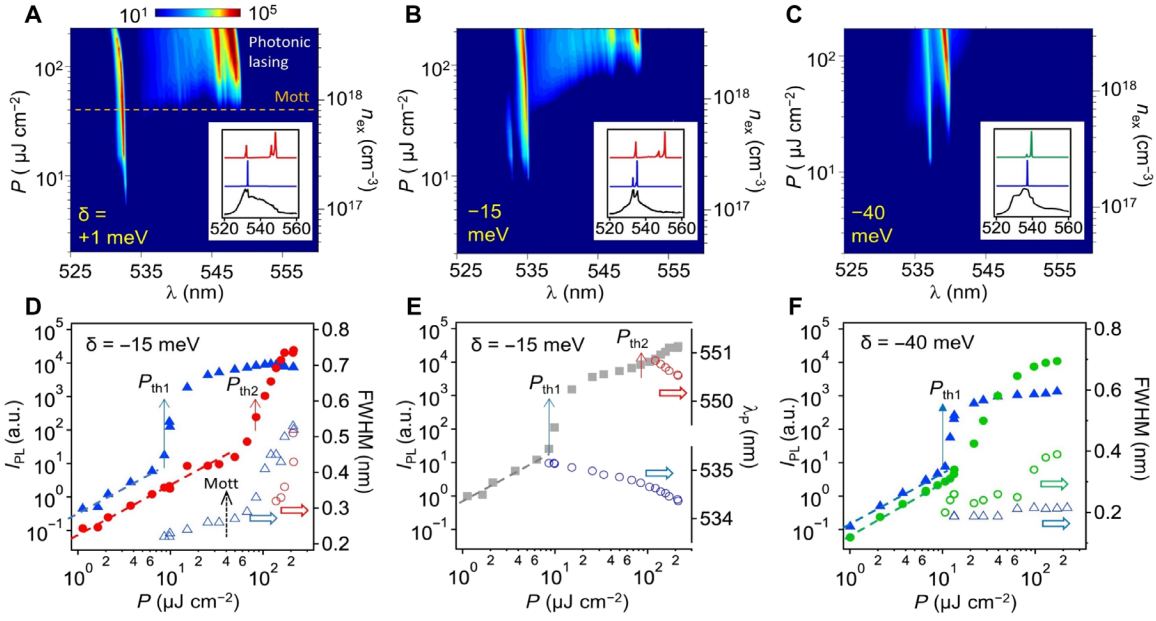

Fig. 3. Condensation of SOC exciton-polaritons in $CsPbBr_3$ microcavities at 77 K. (**A** to **C**) 2D pseudo-color plots of PL spectra as functions of pump fluence (*P*; left axis) or exciton density (n_{ex}; right axis) of three $CsPbBr_3$ microcavities with cavity detuning δ = (A) +1, (B) −15, and (C) −40 meV, respectively. The golden-dashed line in (A) marks the Mott density. Insets in (A) to (C) show normalized PL spectra at three pump fluences: (A) *P* = 4.0 (black), 5.7 (blue), and 108 (red) μJ cm^{-2}; (B) *P* = 1.6 (black), 9.7 (blue), and 170 (red) μJ cm^{-2}; (C) *P* = 6.5 (black), 13 (blue), and 97 (green) μJ cm^{-2}. (**D**) Integrated PL intensity (left axis) as a function of *P* in a log-log scale for the main lasing peaks (blue solid triangles, 531 to 536 nm; red solid circles, 545 to 552 nm), showing the two-threshold behavior for the δ = −15 meV cavity. Also shown are the FWHMs (right axis) of the lasing peaks at ~535 nm (blue open triangles) and ~550 nm (red open circles). a.u., arbitrary units. (**E**) Total PL intensity (525 to 555 nm) (gray squares, left axis) and lasing peak positions (open circles, right axis) as a function of *P* for the δ = −15 meV cavity. (**F**) *P* dependences of integrated PL intensities (left axis) of the two lasing peaks (blue solid triangles, 534 to 538 nm; green solid circles, 538 to 541 nm) and corresponding peak FWHMs (right axis; blue open triangles, ~537 nm; and green open circles, ~540 nm) for the δ = −40 meV cavity.

density further increases and the e-h pair is no longer Coulomb correlated, the mechanism transitions to photonic lasing, i.e., stimulated emission from a degenerate e-h plasma (*40*). The gain mechanisms of both BCS polariton lasing and photonic lasing follow fermionic statistics, as opposed to bosonic statistics in the BEC-type polariton lasing (*39*). However, unambiguously distinguishing BCS polariton lasing from photonic lasing above the second threshold is challenging (*39*), and we leave this as a subject for future experimental and theoretical investigation.

In conventional semiconductor microcavities, stimulated emission from e-h plasmas usually comes from the same cavity mode that forms the polariton condensates. However, the multiple polariton modes of our samples give rise to distinct transition behavior, i.e., the stimulated emission occurs in the next lower-energy cavity mode. This interpretation is supported by analysis of *P*-dependent lasing peak positions, FWHM, and dispersions. We focus on the cavity with δ = −15 meV (see fig. S17 for δ = +1 and −40 meV) and plot the *P*-dependent individual lasing peak intensities and FWHMs in Fig. 3D and peak positions (λ_P) and total PL intensity in Fig. 3E. Above P_{th1}, the intensity of polariton lasing at ~533 nm rises rapidly by over two orders of magnitude in a small *P* window (1 to 4 × P_{th1}), followed by a slow rise and a plateau. Above P_{th2}, the red-shifted stimulated emission lasing peaks at ~548 nm rise rapidly, by a similar rate as that of the polariton lasing peak. The nonlinear increases in lasing intensity above both thresholds are accompanied by blue shifts with increasing *P* (Fig. 3E). Above P_{th1}, repulsive polariton-polariton interaction induces the blue shift (*45*), while above P_{th2}, the blue shift can be attributed to cavity mode renormalization as a result of carrier density–dependent reduction in the refractive index (*40*). The effect of a Mott transition is also evident in FWHM (open symbols in Fig. 3D). While the FWHM of the polariton lasing peak increases with *P*, the rate of increase accelerates above n_{Mott} and is similar to the rate of increase in FWHM for the stimulated emission lasing peak above P_{th2}. The appearance of the additional lasing peaks that are strongly red-shifted and mode hopped to the next lower-lying cavity modes is consistent with the stimulated emission from e-h plasmas involving the emission of plasmons (*40*). An alternative interpretation of the two-threshold behavior is multimode polariton lasing, where polariton lasing may switch modes with increasing excitation density, giving rise to distinct thresholds due to the different relaxation dynamics (*46*). However, our observation of the second threshold being above n_{Mott} and the likely transition into weak coupling disfavors this interpretation. For comparison, we also show in fig. S18 results for a room temperature $CsPbBr_3$ microcavity, where only one lasing threshold near n_{Mott} is observed, suggesting the transition to weak coupling across the threshold. Note that the FWHMs of the lower-energy polariton lasing peaks also increases dramatically when the exciton density exceeds n_{Mott} (Fig. 3, D and F) and are likely indicative of transition to stimulated emission.

Further evidence for polariton condensation comes from power-dependent dispersions (Fig. 4). At $P \sim 0.5P_{th1}$ (Fig. 4A_1), emissions from the two high-energy spin-split polariton modes closest to E_{ex} are the strongest at $\boldsymbol{k}_{||} = 0$ and decrease monotonically with increasing

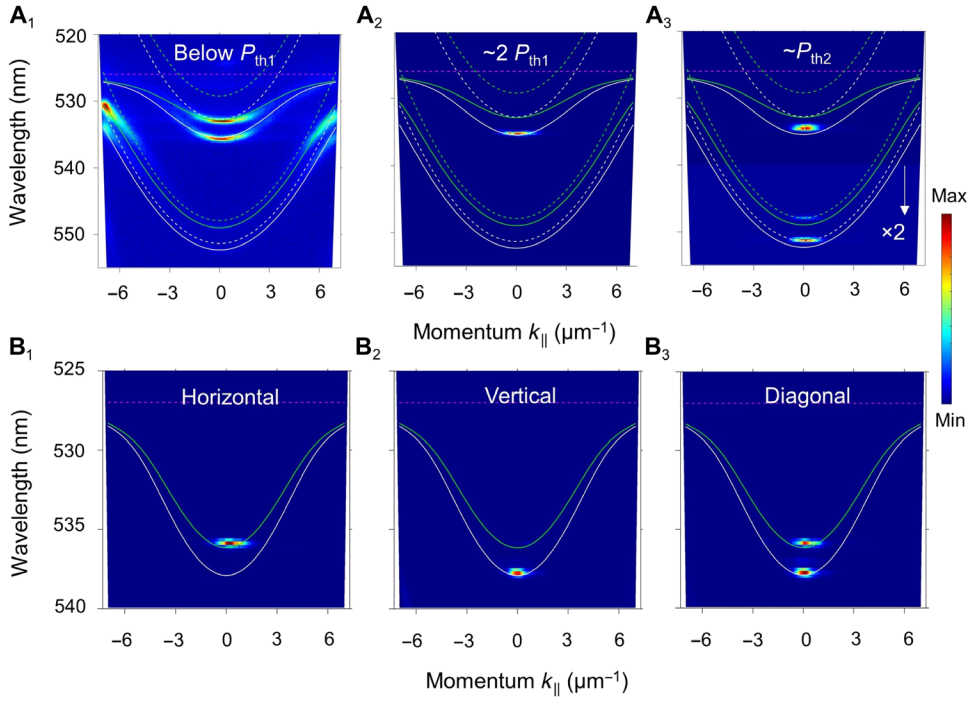

Fig. 4. Competing polariton condensates with orthogonal polarizations at 77 K. (**A**) Angle-resolved PL spectra of a $CsPbBr_3$ microcavity measured at $(A_1) \sim 0.5P_{th1}$, $(A_2) \sim 2P_{th1}$, and $(A_3) \sim P_{th2}$. The cavity detunings are −18 and −98 meV for the higher-energy (~534 nm) and lower-energy (~550 nm) polariton modes, respectively. (**B**) Angle-resolved PL spectra of a $CsPbBr_3$ microcavity with the cavity detuning of −35 meV measured above P_{th1} with the PL polarization along horizontal (B_1), vertical (B_2), and diagonal (B_3) direction with respect to the entrance slit of the spectrometer. The ⟨100⟩ axis of pseudo-cubic perovskite structure is aligned parallel to the entrance slit of the spectrometer. Dashed curves are the expected optical cavity dispersions; solid curves are the model polariton dispersions.

$\boldsymbol{k}_{||}$. By contrast, emissions from the lower-energy polaritons with large detuning are confined to the bottleneck region at high $\boldsymbol{k}_{||}$. When P is above P_{th1} (Fig. $4A_2$), emission occurs exclusively at $\boldsymbol{k}_{||} = 0$, accompanied by a stepwise rise in intensity, a marked peak narrowing, and a blue shift with increasing P (see Fig. 3), as expected for exciton-polariton condensation. When P is increased to $\sim P_{th2}$ (Fig. $4A_3$) the lasing peak near the excitonic resonance is broadened and further blue-shifted. Additional red-shifted lasing peaks emerge and attributed to the photonic lasing mechanism accompanied by plasmon emission.

DISCUSSION

While the $\vec{\boldsymbol{B}}$ fields do not determine the condensation dynamics, they are responsible for the pseudospins of the exciton-polaritons evolve as they undergo Bose scattering down the LBP and undergo phase transitions to the condensates. Below the condensation threshold, $\vec{\boldsymbol{B}}_{XY}$ and $\vec{\boldsymbol{B}}_{T}$ both contribute to give the spin textures at finite $\boldsymbol{k}_{||}$, as exemplified near the diabolic point in Fig. 1H. As the system approaches condensation, population builds up around $\boldsymbol{k}_{||} = 0$ and the spin texture evolves to one dominantly resulting from $\vec{\boldsymbol{B}}_{XY}$, i.e., two orthogonally polarized polaritons illustrated in Fig. 1G. This is most obvious when the magnitude of detuning allows polariton condensation into a pair of spin-split modes with similar intensities (Fig. 4B). Compared to conventional semiconductor microcavities, the orders of magnitude larger anisotropy in our samples can give rise to two competing condensates with different energies. The polarizations of the two condensates are determined by $\vec{\boldsymbol{B}}_{XY}$, not the stochastic condensate polarizations in conventional microcavity exciton-polariton condensates (*47*, *48*). The competing condensation dynamics can be understood from the balance between thermodynamics and kinetics. The lower-energy anisotropic mode is thermodynamically favored, while the higher-energy anisotropic mode is kinetically favored. The kinetic argument can be understood from the smaller curvature along the path toward minimum for the lower-energy mode than that for the higher-energy one, leading to a more efficient scattering pathway toward $\boldsymbol{k}_{||} = 0$ in the former (*49*). While the competition between the two spin-polarized modes is always present because of the thermodynamic and kinetic factors, we find that modest detuning (δ~20 to 40 meV) makes this competition most obvious in the simultaneous presence of both modes. Too small a detuning minimizes the effective field (discussion in text S1), and too large a detuning diminishes the difference in scattering pathways, leading to preferential condensation in the thermodynamically favored mode.

Our discovery of competing exciton-polariton condensates in anisotropic LHP microcavities with artificial and tunable gauge fields offers exciting opportunities for the exploration and simulation of many-body SOC physics in the quantum fluid phase. While we demonstrate the gauge field and the interesting Rashba-Dresselhaus Hamiltonian for exciton-polaritons at finite $\boldsymbol{k}_{||}$ near the diabolic point (Fig. 1), condensation (Figs. 2 to 4) occurs at $\boldsymbol{k}_{||} = 0$ where $\vec{B}_T = 0$ and the effective magnetic field results exclusively from $\vec{B}_{XY}$. As an exciting future research direction, we may systematically tune the relative amplitude of $\vec{B}_T$ and, thus, the gauge field and experimentally access momentum space away from $\boldsymbol{k}_{||} = 0$, particularly near the

diabolic point. This is possible from off-normal and resonant optical excitation to launch propagating exciton-polaritons and condensates. Theory predicts that, for these propagating SOC condensates in a finite $k_{||}$ range above or below the diabolic point, the gauge field can result in dynamic instability, spin-textured phase separation, and strip formation in the quantum fluid (*10*). Our finding provides a starting point for the experimental exploration of a range of phenomena in SOC quantum fluids in a solid state and high-temperature model system, as done previously in cold atom–based SOC-BECs (*19*–*21*).

MATERIALS AND METHODS

Microcavity fabrication

All chemicals and regents were purchased from Sigma-Aldrich and used as received, unless noted otherwise. $CsPbBr_3$ precursor solution with a concentration of 0.4 M was prepared by dissolving stoichiometric 1:1 CsBr and $PbBr_2$ in dimethyl sulfoxide. $MAPbBr_3$ precursor solution with a concentration of 1.0 M was prepared by dissolving stoichiometric 1:1 MABr and $PbBr_2$ in dimethylformamide. Two types of DBRs were used to fabricate the microcavities studied here. One type of DBR consists of pairs of alternating silicon dioxide and silicon nitride, which were deposited on quartz or silicon wafers on an Oxford PlasmaPro PECVD NPG80 instrument. The center of the stop band was measured at 544 nm with a band width of 108 nm. The other type was custom-produced by Thorlabs (subtractive magenta dichoric filter), and the center of the stop band was measured at 545 nm with a band width of 160 nm. Two opposing DBRs were bonded by epoxy, forming an empty cavity. Perovskite solutions were filled into the cavity through capillary action. The microcavity was then placed in a fused silica tube mounted in a single-zone Lindberg/Blue M tube furnace and connected to vacuum pump. The pressure in the tube was ~27 mtorr, and the furnace temperature was ~80°C. The solvent in the cavity slowly evaporated to form single-crystal perovskites within a few days. Representative optical images of $MAPbBr_3$ and $CsPbBr_3$ are shown in fig. S1.

Structural characterization

The powder x-ray diffraction data were collected on as-grown samples using a Bruker D8 Advance powder x-ray diffractometer with Cu Kα radiation. The atomic force microscopy measurements were performed using a Bruker Dimension FastScan atomic force microscope.

Spectroscopic characterization

Angle-resolved PL measurements were carried out on a home-built confocal setup (see fig. S5 for the details of the setup). The reflectance spectra of the crystals were measured with the same setup using a white lamp source. Low-temperature PL measurements were performed in a cryostat (Cryo Industries of America, RC102-CFM Microscopy Cryostat with LakeShore 325 Temperature Controller). The cryostat was operated at pressures $<10^{-7}$ mbar (pumped by a Varian turbo pump) and cooled with flow-through liquid nitrogen. The second harmonic of a Clark-MXR Impulse laser (repetition rate of 0.5 MHz, 250-fs pulses, and 1040 nm), and a white-light signal generated via CaF_2 and Impulse laser fundamental, was used to pump a home-built noncollinear optical parametric amplifier to generate 800-nm pulses, which was used to generate 400-nm pulses via second harmonic generation. The beam size is expanded to ensure large-area illumination with a spot size ~25 μm and focused onto the sample with a far-field epifluorescence microscope (Olympus, IX73 inverted microscope) equipped with a ×40 objective with a numerical aperture of 0.6, with correction collar (Olympus LUCPLFLN40X) and a 490-nm long-pass dichroic mirror (Thorlabs, DMPL490R). The emission spectra were collected with a liquid nitrogen–cooled charge-coupled device (Princeton Instruments, PyLoN 400B) coupled to a spectrograph (Princeton Instruments, Acton SP 2300i). We used the Lightfield software suite (Princeton Instruments) and LabVIEW (National Instruments) in data collection.

Carrier density estimation

We estimated the exciton density in photoexcited LHP single crystals using the following equation

$$n_{3D} = \frac{(1-R)(1-A_{DBR})A_{PVK}P}{f_{rep}\hbar\omega\pi r^2 d} \quad (6)$$

in which n_{3D} is the exciton density, R is the reflectivity of microcavity, A_{DBR} is the absorbance of top DBR, A_{PVK} is the absorbance of the perovskite crystal, P is the average power from the pulsed pump laser, f_{rep} is the repetition rate of the pump laser, $\hbar\omega$ is the photon energy of the pump laser, πr^2 is the area of the pump spot, and $d \sim 1$ μm is the thickness of the perovskite crystal (fig. S3). Assuming negligible reflectivity and negligible absorbance of the top DBR, and unity absorbance of the perovskite crystal, the upper limit of the carrier density at the first threshold (~5.0 μJ cm^{-2}) is estimated to be $\sim 1.0 \times 10^{17}$ cm^{-3}, and the one at the second threshold (~53 μJ cm^{-2}) is $\sim 1.1 \times 10^{18}$ cm^{-3}.

We note that while the carrier density estimations in polariton systems may have large uncertainties, they can serve as an important check of the Mott transition. In our experiment, we observed unambiguous spectral signatures of the Mott transition above the second threshold: (i) a second threshold appears, (ii) the photon lasing hops to the next, lower-energy cavity modes due to plasmon emission, and (iii) the photon lasing transition is accompanied by significant linewidth broadening and apparent blue shift of the lasing peak, which are consistent with the disappearance of a bound excitonic state.

SUPPLEMENTARY MATERIALS

Supplementary material for this article is available at https://science.org/doi/10.1126/sciadv.abj7667

REFERENCES AND NOTES

1. M. I. Dyakonov, V. I. Perel, Current-induced spin orientation of electrons in semiconductors. *Phys. Lett. A* **35**, 459–460 (1971).
2. M. Z. Hasan, C. L. Kane, Colloquium: Topological insulators. *Rev. Mod. Phys.* **82**, 3045–3067 (2010).
3. K. Rechcińska, M. Król, R. Mazur, P. Morawiak, R. Mirek, K. Łempicka, W. Bardyszewski, M. Matuszewski, P. Kula, W. Piecek, P. G. Lagoudakis, B. Pietka, J. Szczytko, Engineering spin-orbit synthetic Hamiltonians in liquid-crystal optical cavities. *Science* **366**, 727–730 (2019).
4. A. Kavokin, G. Malpuech, M. Glazov, Optical spin Hall effect. *Phys. Rev. Lett.* **95**, 136601 (2005).
5. C. Leyder, M. Romanelli, J. P. Karr, E. Giacobino, T. C. H. Liew, M. M. Glazov, A. V. Kavokin, G. Malpuech, A. Bramati, Observation of the optical spin Hall effect. *Nat. Phys.* **3**, 628–631 (2007).
6. X. Yin, Z. Ye, J. Rho, Y. Wang, X. Zhang, Photonic spin hall effect at metasurfaces. *Science* **339**, 1405–1407 (2013).
7. A. Gianfrate, O. Bleu, L. Dominici, V. Ardizzone, M. De Giorgi, D. Ballarini, G. Lerario, K. W. West, L. N. Pfeiffer, D. D. Solnyshkov, D. Sanvitto, G. Malpuech, Measurement of the quantum geometric tensor and of the anomalous Hall drift. *Nature* **578**, 381–385 (2020).
8. C. E. Whittaker, T. Dowling, A. V. Nalitov, A. V. Yulin, B. Royall, E. Clarke, M. S. Skolnick, I. A. Shelykh, D. N. Krizhanovskii, Optical analogue of Dresselhaus spin–orbit interaction in photonic graphene. *Nat. Photonics* **15**, 193–196 (2021).

9. C. Sturm, H. Hilmer, B. Rheinländer, R. Schmidt-Grund, M. Grundmann, Cavity-photon dispersion in one-dimensional confined microresonators with an optically anisotropic cavity material. *Phys. Rev. B* **83**, 205301 (2011).
10. H. Terças, H. Flayac, D. D. Solnyshkov, G. Malpuech, Non-Abelian gauge fields in photonic cavities and photonic superfluids. *Phys. Rev. Lett.* **112**, 66402 (2014).
11. C. E. Whittaker, E. Cancellieri, P. M. Walker, D. R. Gulevich, H. Schomerus, D. Vaitiekus, B. Royall, D. M. Whittaker, E. Clarke, I. V. Iorsh, I. A. Shelykh, M. S. Skolnick, D. N. Krizhanovskii, Exciton polaritons in a two-dimensional lieb lattice with spin-orbit coupling. *Phys. Rev. Lett.* **120**, 097401 (2018).
12. V. G. Sala, D. D. Solnyshkov, I. Carusotto, T. Jacqmin, A. Lemaître, H. Terças, A. Nalitov, M. Abbarchi, E. Galopin, I. Sagnes, J. Bloch, G. Malpuech, A. Amo, Spin-orbit coupling for photons and polaritons in microstructures. *Phys. Rev. X* **5**, 11034 (2015).
13. S. Klembt, T. H. Harder, O. A. Egorov, K. Winkler, R. Ge, M. A. Bandres, M. Emmerling, L. Worschech, T. C. H. Liew, M. Segev, C. Schneider, S. Höfling, Exciton-polariton topological insulator. *Nature* **562**, 552–556 (2018).
14. R. Su, E. Estrecho, D. Biegańska, Y. Huang, M. Wurdack, M. Pieczarka, A. G. Truscott, T. C. H. Liew, E. A. Ostrovskaya, Q. Xiong, Direct measurement of a non-hermitian topological invariant in a hybrid light-matter system. arXiv:2012.06133 [physics. optics] (11 December 2020).
15. L. Polimeno, M. De Giorgi, G. Lerario, L. De Marco, L. Dominici, V. Ardizzone, M. Pugliese, C. T. Prontera, V. Maiorano, A. Moliterni, C. Giannini, V. Olieric, G. Gigli, *D. Ballarini*, D. Solnyshkov, G. Malpuech, D. Sanvitto, Tuning the Berry curvature in 2D Perovskite. arXiv:2007.14945 [physics.optics] (29 July 2020).
16. J. Ren, Q. Liao, F. Li, Y. Li, O. Bleu, G. Malpuech, J. Yao, H. Fu, D. Solnyshkov, Nontrivial band geometry in an optically active system. *Nat. Commun.* **12**, 689 (2021).
17. J. Kasprzak, M. Richard, S. Kundermann, A. Baas, P. Jeambrun, J. M. J. Keeling, F. M. Marchetti, M. H. Szymánska, R. André, J. L. Staehli, V. Savona, P. B. Littlewood, B. Deveaud, L. S. Dang, Bose-Einstein condensation of exciton polaritons. *Nature* **443**, 409–414 (2006).
18. T. Byrnes, N. Y. Kim, Y. Yamamoto, Exciton-polariton condensates. *Nat. Phys.* **10**, 803–813 (2014).
19. Y.-J. Lin, K. Jiménez-García, I. B. Spielman, Spin–orbit-coupled Bose–Einstein condensates. *Nature* **471**, 83–86 (2011).
20. L. E. Sadler, J. M. Higbie, S. R. Leslie, M. Vengalattore, D. M. Stamper-Kurn, Spontaneous symmetry breaking in a quenched ferromagnetic spinor Bose–Einstein condensate. *Nature* **443**, 312–315 (2006).
21. J.-R. Li, J. Lee, W. Huang, S. Burchesky, B. Shteynas, F. Ç. Top, A. O. Jamison, W. Ketterle, A stripe phase with supersolid properties in spin–orbit-coupled Bose–Einstein condensates. *Nature* **543**, 91–94 (2017).
22. Y. Fu, H. Zhu, J. Chen, M. P. Hautzinger, X.-Y. Zhu, S. Jin, Metal halide perovskite nanostructures for optoelectronic applications and the study of physical properties. *Nat. Rev. Mater.* **4**, 169–188 (2019).
23. A. Fieramosca, L. Polimeno, V. Ardizzone, L. De Marco, M. Pugliese, V. Maiorano, M. De Giorgi, L. Dominici, G. Gigli, D. Gerace, D. Ballarini, D. Sanvitto, Two-dimensional hybrid perovskites sustaining strong polariton interactions at room temperature. *Sci. Adv.* **5**, eaav9967 (2019).
24. R. Su, J. Wang, J. Zhao, J. Xing, W. Zhao, C. Diederichs, T. C. H. Liew, Q. Xiong, Room temperature long-range coherent exciton polariton condensate flow in lead halide perovskites. *Sci. Adv.* **4**, eaau0244 (2018).
25. W. Bao, X. Liu, F. Xue, F. Zheng, R. Tao, S. Wang, Y. Xia, M. Zhao, J. Kim, S. Yang, Q. Li, Y. Wang, Y. Wang, L. W. Wang, A. H. MacDonald, X. Zhang, Observation of Rydberg exciton polaritons and their condensate in a perovskite cavity. *Proc. Natl. Acad. Sci. U.S.A.* **116**, 20274–20279 (2019).
26. R. Su, C. Diederichs, J. Wang, T. C. H. Liew, J. Zhao, S. Liu, W. Xu, Z. Chen, Q. Xiong, Room-temperature polariton lasing in all-inorganic perovskite nanoplatelets. *Nano Lett.* **17**, 3982–3988 (2017).
27. R. Su, S. Ghosh, J. Wang, S. Liu, C. Diederichs, T. C. H. Liew, Q. Xiong, Observation of exciton polariton condensation in a perovskite lattice at room temperature. *Nat. Phys.* **16**, 301–306 (2020).
28. R. Su, S. Ghosh, T. C. H. Liew, Q. Xiong, Optical switching of topological phase in a perovskite polariton lattice. *Sci. Adv.* **7**, eabf8049 (2021).
29. S. F. Maehrlein, P. P. Joshi, L. Huber, F. Wang, M. Cherasse, Y. Liu, D. M. Juraschek, E. Mosconi, D. Meggiolaro, F. De Angelis, X.-Y. Zhu, Decoding ultrafast polarization responses in lead halide perovskites by the two-dimensional optical Kerr effect. *Proc. Natl. Acad. Sci. U.S.A.* **118**, e2022268118 (2021).
30. F. Tassone, C. Piermarocchi, V. Savona, A. Quattropani, P. Schwendimann, Bottleneck effects in the relaxation and photoluminescence of microcavity polaritons. *Phys. Rev. B* **56**, 7554–7563 (1997).
31. G. Panzarini, L. C. Andreani, A. Armitage, D. Baxter, M. S. Skolnick, V. N. Astratov, J. S. Roberts, A. Kavokin, M. Vladimirova, M. A. Kaliteevski, Exciton-light coupling in single and coupled semiconductor microcavities: Polariton dispersion and polarization splitting. *Phys. Rev. B* **59**, 5082–5089 (1999).
32. S. Donati, L. Dominici, G. Dagvadorj, D. Ballarini, M. De Giorgi, A. Bramati, G. Gigli, Y. G. Rubo, M. H. Szymańska, D. Sanvitto, Twist of generalized skyrmions and spin vortices in a polariton superfluid. *Proc. Natl. Acad. Sci. U.S.A.* **113**, 14926–14931 (2016).
33. M. Kłopotowski, D. Martín, A. Amo, L. Viña, I. A. Shelykh, M. M. Glazov, G. Malpuech, A. V. Kavokin, R. André, Optical anisotropy and pinning of the linear polarization of light in semiconductor microcavities. *Solid State Commun.* **139**, 511–515 (2006).
34. Y. Guo, O. Yaffe, T. D. Hull, J. S. Owen, D. R. Reichman, L. E. Brus, Dynamic emission Stokes shift and liquid-like dielectric solvation of band edge carriers in lead-halide perovskites. *Nat. Commun.* **10**, 1175 (2019).
35. M. Yamaguchi, K. Kamide, R. Nii, T. Ogawa, Y. Yamamoto, Second thresholds in BEC-BCS-laser crossover of exciton-polariton systems. *Phys. Rev. Lett.* **111**, 026404 (2013).
36. J. S. Tempel, F. Veit, M. Aßmann, L. E. Kreilkamp, A. Rahimi-Iman, A. Löffler, S. Höfling, S. Reitzenstein, L. Worschech, A. Forchel, M. Bayer, Characterization of two-threshold behavior of the emission from a GaAs microcavity. *Phys. Rev. B* **85**, 075318 (2012).
37. H. Deng, G. Weihs, D. Snoke, J. Bloch, Y. Yamamoto, Polariton lasing vs. photon lasing in a semiconductor microcavity. *Proc. Natl. Acad. Sci.* **100**, 15318–15323 (2003).
38. C. P. Dietrich, A. Steude, L. Tropf, M. Schubert, N. M. Kronenberg, K. Ostermann, S. Höfling, M. C. Gather, An exciton-polariton laser based on biologically produced fluorescent protein. *Sci. Adv.* **2**, e1600666 (2016).
39. J. Hu, Z. Wang, S. Kim, H. Deng, S. Brodbeck, C. Schneider, S. Höfling, N. H. Kwong, R. Binder, Polariton laser in the Bardeen-Cooper-Schrieffer regime. *Phys. Rev. X* **11**, 011018 (2021).
40. A. P. Schlaus, M. S. Spencer, K. Miyata, F. Liu, X. Wang, I. Datta, M. Lipson, A. Pan, X.-Y. Zhu, How lasing happens in CsPbBr3 perovskite nanowires. *Nat. Commun.* **10**, 265 (2019).
41. T. Palmieri, E. Baldini, A. Steinhoff, A. Akrap, M. Kollár, E. Horváth, L. Forró, F. Jahnke, M. Chergui, Mahan excitons in room-temperature methylammonium lead bromide perovskites. *Nat. Commun.* **11**, 850 (2020).
42. J. Keeling, P. R. Eastham, M. H. Szymanska, P. B. Littlewood, BCS-BEC crossover in a system of microcavity polaritons. *Phys. Rev. B* **72**, 115320 (2005).
43. K. Kamide, T. Ogawa, What determines the wave function of electron-hole pairs in polariton condensates? *Phys. Rev. Lett.* **105**, 56401 (2010).
44. T. Byrnes, T. Horikiri, N. Ishida, Y. Yamamoto, BCS wave-function approach to the BEC-BCS crossover of exciton-polariton condensates. *Phys. Rev. Lett.* **105**, 186402 (2010).
45. H. Deng, H. Haug, Y. Yamamoto, Exciton-polariton Bose-Einstein condensation. *Rev. Mod. Phys.* **82**, 1489–1537 (2010).
46. W. Xie, H. Dong, S. Zhang, L. Sun, W. Zhou, Y. Ling, J. Lu, X. Shen, Z. Chen, Room-temperature polariton parametric scattering driven by a one-dimensional polariton condensate. *Phys. Rev. Lett.* **108**, 166401 (2012).
47. J. Levrat, R. Butté, T. Christian, M. Glauser, E. Feltin, J. F. Carlin, N. Grandjean, D. Read, A. V. Kavokin, Y. G. Rubo, Pinning and depinning of the polarization of exciton-polariton condensates at room temperature. *Phys. Rev. Lett.* **104**, 166402 (2010).
48. I. A. Shelykh, Y. G. Rubo, G. Malpuech, D. D. Solnyshkov, A. Kavokin, Polarization and propagation of polariton condensates. *Phys. Rev. Lett.* **97**, 066402 (2006).
49. J. Kasprzak, D. D. Solnyshkov, R. Andre, L. S. Dang, G. Malpuech, Formation of an exciton polariton condensate: Thermodynamic versus kinetic regimes. *Phys. Rev. Lett.* **101**, 146404 (2008).

Acknowledgments

Funding: This work was solely supported by the Center of Programmable Quantum Materials (Pro-QM), an Energy Frontier Research Center of the U.S. Department of Energy under grant number DE-SC0019443. We thank the help on sample preparation by S. Jin, K. J. Lee, and O. Bakr. **Author contributions:** X.-Y.Z., M.S.S., and Y.F. conceived this work. M.S.S. and Y.F. performed all optical experiments presented here. M.S.S. built the experimental setup, with assistance from A.P.S. and Y.D. Y.F. carried out sample fabrication, with inputs at the initial stage of this research project from D.H., M.D.S., and D.R.G. Y.F., M.S.S, and X.-Y.Z. wrote the manuscript, with inputs from all coauthors. X.-Y.Z. supervised the project. All authors participated in the discussion and interpretation of the results. **Competing interests:** The authors declare that they have no competing interests. **Data and materials availability:** All data needed to evaluate the conclusions in the paper are present in the paper or the Supplementary Materials.

Submitted 31 May 2021
Accepted 12 October 2021
Published 1 December 2021
10.1126/sciadv.abj7667